The impact of channel assembled angle on proton exchange membrane fuel cell performance

Yi Han, Jie-Min Zhan*

Department of Applied Mechanics and Engineering, SunYat-sen University, Guangzhou 510275, PR China

ARTICLE INFO

ABSTRACT

A three-dimensional, two-phase, multi-component model is used to investigate the effects of channel assembled angle on the performance of proton exchange membrane (PEM) fuel cell, including distribution of current density, membrane water content and local temperature. The flow-fields are assembled by single serpentine channels in anode and cathode with intersection angles of 0°, 90°, 180° and 270°, respectively. At high inlet humidity condition each flow-field has its owned strengths. Flow-fields with channel assembled angles of 0°, 90° and 270° show most uniform membrane water content, current density and local temperature distributions, respectively. However, at low inlet humidity condition, flow-field with channel assembled angle of 90° represents highest performance and uniformities in all aspects. Flow-field design for PEM fuel cell should take into account the effects of channel assembled angle on cell performance.

© 2010 Elsevier B.V. All rights reserved.

1. Introduction

Proton exchange membrane (PEM) fuel cell is a type of clean energy developed for vehicles, stationary applications and portable devices. Its distinguishing features include quick start-up capability, high power density, low operating temperature, low emission and robust system. In PEM fuel cell systems, bipolar plates are used to connect single fuel cells together and increase the output power. Moreover, flow channels on bipolar plates play an important role in distributing gas reactants over the membrane electrode assembly (MEA). A uniform distribution of reactants should cause uniform distribution of reaction rate, which results in uniform distributions of current density, temperature and liquid water production over the area of the cell [1,2]. Furthermore, these uniformities can lead to less stresses on the MEA and thus extend the lifetime of the cell [2].

Nowadays there exist several flow-field patterns included the pin-type, straight or parallel, serpentine, and interdigitated designs [3]. These various designs have their own advantages and disadvantages that make them suitable for different applications. Many researchers have studied the effects of various flow-field designs on the performance of fuel cells. Fell et al. [4] studied the pressure drop over the cathode flow-field and its influences on the current density distribution, and proposed the cyclic-single and symmetric-single channel flow-fields. Glandt et al. [5] compared characteristics

of a single serpentine channel flow-field with a double channel one. They reported that changing the flow-field configuration can affect the current density distribution and cell performance. Hu et al. [6] employed a steady-state, three-dimensional mathematical model to compare the characteristics within the interdigitated and parallel flow-fields. Su et al. [7] studied the gas concentration distribution within the straight and serpentine flow patterns and their influences on the cell performance. Li et al. [8] used experimental method to compare cell performance between serpentine and pin-type flow-fields. Shimpalee et al. [1] investigated on five flow-fields. They reported that changing flow-field configuration by varying path length by changing the number of parallel channels can affect cell performance and uniformity. Karvonen et al. [9] proposed a parallel channel flow-field with nearly uniform distribution through experimental and numerical methods. Jeon et al. [2] studied on four kinds of serpentine flow-field configurations under different humidity conditions. They also pointed out the advantages and disadvantages of the flow-fields, respectively. Li and Sabir [3] reviewed the flow-field layouts developed by different companies and research groups, and presented the pros and cons associated with these designs. Kloess et al. [10] summarized several flow-field designs over the past years and proposed two new flow patterns with inspiration from natural flow-fields. They reported that both of the leaf and lung flow patterns showed improvements over previous designs by up to 30% in peak power density.

The main objective of flow-field design is to increase uniformity of the current density, temperature and liquid water distributions under the desired operating conditions while maintaining or improving polarization. So far most of the research works in flow-

* Corresponding author. Tel.: +86 20 8411 1130; fax: +86 20 8411 1130.
E-mail address: cejmzhan@gmail.com (J.-M. Zhan).

Nomenclature

a	water activity
A_p	surface area of the porous medium (m^2)
C_p	specified heat ($J\,kg^{-1}\,K^{-1}$)
C_q	quadratic drag factor
d_p	equivalent pore diameter of the porous medium (m)
D	mass diffusivity ($m^2\,s^{-1}$)
D^{eff}	effective diffusion coefficient ($m^2\,s^{-1}$)
D_b^{diff}	back diffusion flux ($kg\,m^{-3}$)
D_m	membrane water diffusivity
F	Faraday constant ($96,487\,C\,mol^{-1}$)
h_w	enthalpy of formation for water (J)
i	current density ($A\,m^{-2}$)
j^{ref}	reference exchange current density per active surface area ($A\,m^{-2}$)
J	transfer current density ($A\,m^{-2}$)
J_{echm}	Joule heating (J)
M	molecular weight ($kg\,mol^{-1}$)
M_{mem}	equivalent weight of dry membrane ($kg\,mol^{-1}$)
n_d	osmotic drag coefficient
p	local pressure (atm)
p_c	capillary pressure (atm)
p_{wv}	water vapor pressure (atm)
R	universal gas constant ($8.314\,J\,mol^{-1}\,K^{-1}$)
s	volume fraction of liquid water
S_d	source term in the momentum equation
S_m	source term due to phase change of water
S_p	source term in the species equation
T	temperature (K)
$\vec{u}$	velocity vector ($m\,s^{-1}$)
V_{cell}	operating voltage (V)
V_{oc}	open-circuit voltage (V)
V_p	volume of the porous medium (m^3)
X	mole fraction
X^{ref}	reference mole fraction
Y	mass fraction

Greek letters

α	transfer coefficient
γ	concentration exponent
ε	porosity
ζ	specific active surface area (m^{-1})
η	overpotential (V)
θ_c	contact angle of water on the porous medium (arc)
κ_c	coefficient of water vapor condensation rate
κ_e	coefficient of water vapor evaporation rate
κ_{eff}	effective thermal conductivity ($W\,m^{-1}\,K^{-1}$)
κ_p	permeability of the porous medium (m^2)
κ_{rg}	relative permeability for the gas
λ	membrane water content
μ	viscosity ($kg\,m^{-1}\,s^{-1}$)
ρ	density ($kg\,m^{-3}$)
σ	electrical conductivity ($S\,m^{-1}$)
τ	surface tension ($N\,m^{-1}$)
φ_{mem}	membrane phase potential (V)
φ_{sol}	solid phase potential (V)

Subscripts

an	anode
cat	cathode
g	gas
H_2	hydrogen
H_2O	water
i	ith species
l	liquid phase
mem	membrane
O_2	oxygen
sat	saturation

field design are focused on patterns or geometries of the channels and ribs. Furthermore, channels from these works were assembled with intersection angle of $0°$. In the author's opinion, the assembled angle between the anode and cathode channels did not have sufficient discussion before. The goal of this study is to investigate the effects of different channel assembled angles on polarization and distributions of the fuel cells. In this study, four computational models, of which channels in anode and cathode were assembled with intersection angles of $0°$, $90°$, $180°$ and $270°$, respectively, were analyzed (see in Fig. 1(A)). A commercial computational fluid dynamics (CFD) package, FLUENT, was adopted to simulate the three-dimensional flow-fields and other phenomena. Since high inlet humidity is usually applied in stationary applications while low inlet humidity is normally used in portable devices, this paper covers the results and analysis of cell performance under these two conditions.

2. Model development

A three-dimensional, two-phase, multi-component PEM fuel cell model was used to analyze the electrochemical reaction and transport phenomena in this work. The model assumed that the system was steady; the inlet reactants were ideal gases; the flow was laminar; the porous layers were isotropic and isothermal. The model included continuity, momentum, species transport and energy equations. The Butler–Volmer equation was adopted to compute the electrochemical reactions in the catalyst layers. Liquid water formation and transport equations were also employed in the model.

2.1. Governing equations

The continuity equation for the gas is as follows:

$$\nabla \cdot (\varepsilon \rho_g \vec{u}_g) = -S_m \tag{1}$$

where ε is the porosity of the porous medium, ρ_g is the gas density, $\vec{u}_g$ is the velocity vector, and S_m is the source term due to phase change of water which will be discussed later in Eq. (23).

The momentum equation for the gas is as follows:

$$\frac{\varepsilon}{(1-s)^2} \nabla \cdot (\rho_g \vec{u}_g \vec{u}_g) = -\varepsilon \nabla p_g + \frac{\varepsilon}{1-s} \nabla \cdot (\mu_g \nabla \vec{u}_g) + S_d \tag{2}$$

Where s is the volume fraction of liquid water, or water saturation, and μ_g is viscous coefficient of gas. S_d denotes the source terms based on the Darcy's law, representing extra drag forces in the equation as follows:

$$S_d = -\frac{\varepsilon^2 \mu_g \vec{u}_g}{\kappa_p \kappa_{rg}} - \frac{\varepsilon^3 C_q \rho_g}{\sqrt{\kappa_p}} \left| \vec{u}_g \right| \vec{u}_g \tag{3}$$

where κ_{rg} is the relative permeability for the gas, C_q is the quadratic drag factor, and κ_p is the permeability of the porous medium, defined by the Blake–Kozeny equation:

$$\kappa_p = \frac{d_p^2 \varepsilon^3}{150(1-\varepsilon)^2} = \frac{36 V_p^2 \varepsilon^3}{150 A_p^2 (1-\varepsilon)^2} \tag{4}$$
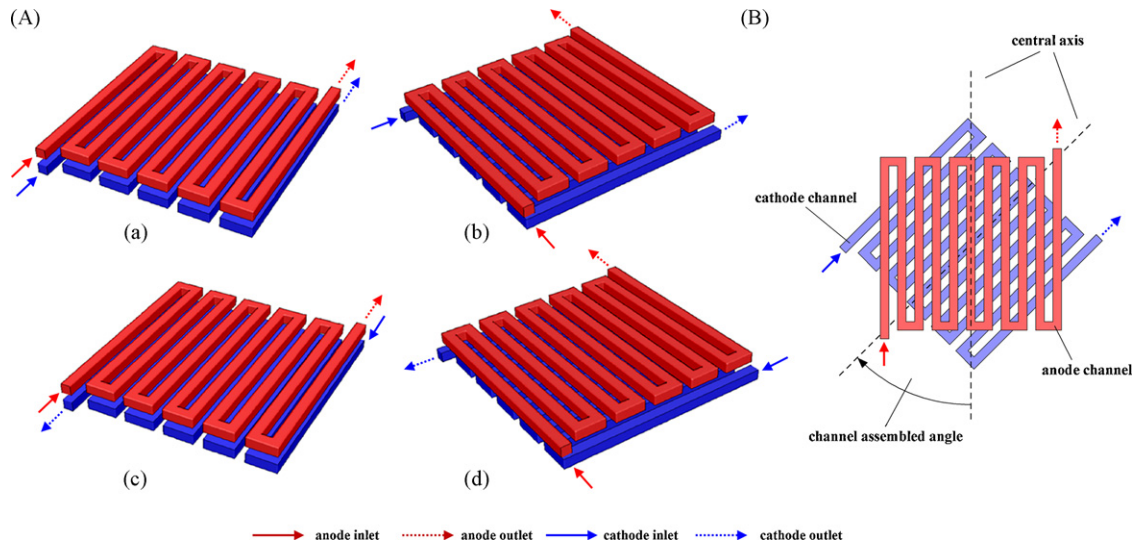
Fig. 1. (A) Schematics of the flow-fields based on single serpentine channels with different channel assembled angles: (a) A-0; (b) A-90; (c) A-180; (d) A-360. (B) Definition of channel assembled angle.

where d_p is the equivalent pore diameter of the porous medium, V_p and A_p are the volume and surface area of the porous medium, respectively.

The species equation for the gas species is as follows:

$$\nabla \cdot (\varepsilon \rho_g \vec{u}_g Y_i) = \nabla \cdot (\rho_g D_i^{eff} Y_i) + S_p - S_m \qquad (5)$$

where Y_i is the mass fraction of species i, and D_i^{eff} is the effective diffusion coefficient corrected by Bruggemann correction [11]:

$$D_i^{eff} = \varepsilon^{1.5} D_i \qquad (6)$$

where $\varepsilon^{1.5}$ is used to model the effect of tortuosity, and D_i is the mass diffusivity of species i. Source term S_p in the catalyst layers denotes as follows:

$$S_p = -\frac{M_{H_2}}{2F} J_{an} \quad \text{for } H_2 \qquad (7)$$

$$S_p = -\frac{M_{O_2}}{4F} J_{cat} \quad \text{for } O_2 \qquad (8)$$

$$S_p = \frac{M_{H_2O}}{2F} J_{cat} \quad \text{for } H_2O \qquad (9)$$

where M_{H_2}, M_{O_2} and M_{H_2O} are the molecular weight of hydrogen, oxygen and water, respectively. The J_{an} and J_{cat} are the transfer current densities at the anode and cathode, respectively. They can be computed with the Butler–Volmer equation:

$$J_{an} = \zeta_{an} j_{an}^{ref} \left(\frac{X_{H_2}}{X_{H_2}^{ref}} \right)^{\gamma_{an}} \left[\exp \left(\frac{\alpha_{an} \eta_{an} F}{RT} \right) - \exp \left(-\frac{\alpha_{cat} \eta_{an} F}{RT} \right) \right] \quad (10)$$

$$J_{cat} = \zeta_{cat} j_{cat}^{ref} \left(\frac{X_{O_2}}{X_{O_2}^{ref}} \right)^{\gamma_{cat}} \left[-\exp \left(\frac{\alpha_{an} \eta_{cat} F}{RT} \right) + \exp \left(-\frac{\alpha_{cat} \eta_{cat} F}{RT} \right) \right] \quad (11)$$

where ζ is the specific active surface area, j^{ref} is the reference exchange current density per active surface area, X^{ref} is the local species reference concentration, γ is the concentration exponent, α is the transfer coefficient, F is the Faraday constant, R is the gas constant and T is the absolute temperature. In the expressions η is the local surface overpotential calculated as follows:

$$\eta_{an} = \varphi_{sol} - \varphi_{mem} \qquad (12)$$

$$\eta_{cat} = \varphi_{sol} - \varphi_{mem} - V_{OC} \qquad (13)$$

where V_{oc} is the open-circuit voltage. The cell voltage is given by:

$$V_{cell} = V_{oc} - \eta_{an} - \eta_{cat} - \eta_{mem} \qquad (14)$$

Table 2
Operating conditions and parameters.

	High inlet humidity	Low inlet humidity
Anode		
Gas	H_2	H_2
Stoichiometry	1.2	1.2
Inlet temperature (K)	353	353
Relative humidity (%)	100	53
Reference exchange current density (A m^{-2})	8000	8000
Concentration exponent	0.5	0.5
Exchange coefficient	2	2
Cathode		
Gas	Air	Air
Stoichiometry	2.0	2.0
Inlet temperature (K)	343	343
Relative humidity (%)	100	64
Reference exchange current density (A m^{-2})	200	200
Concentration exponent	1	1
Exchange coefficient	2	2
Operating conditions		
Inlet pressure (atm)	1.0	1.0
Outlet pressure (atm)	1.0	1.0
Open-circuit voltage (V)	1.10	1.10
Cell temperature (K)	343	343

Table 1
Geometry details and material properties.

Properties	Value
Current collector height (mm)	0.5
Channel width (mm)	1.0
Channel height (mm)	1.0
Rib width (mm)	1.0
Gas diffusion layer thickness (μm)	260
Gas diffusion layer permeability (m^2)	2.55×10^{-13} [21]
Gas diffusion layer porosity	0.5
Catalyst layer thickness (μm)	29
Catalyst layer porosity	0.4
Membrane thickness (μm)	180
Dry membrane density (kg m^{-3})	1980
Equivalent weight of dry membrane (kg mol^{-1})	1100

where η_{mem} is the Ohmic overpotential of the membrane.

The keystone of the electrochemistry is to calculate the anodic and cathodic reactions. The driving force behind these reactions is the difference between the electronic phase potential, φ_{sol}, and the ionic phase potential, φ_{mem}. Therefore, the following two potential equations are solved:

$$\nabla \cdot (\sigma_{sol} \nabla \varphi_{sol}) + J_{sol} = 0 \tag{15}$$

$$\nabla \cdot (\sigma_{mem} \nabla \varphi_{mem}) + J_{mem} = 0 \tag{16}$$

where σ_{sol} is the electron conductivity, and σ_{mem} is the proton conductivity. The source terms J_{sol} and J_{mem} are zero in the PEM fuel cell except inside the catalyst layers. For Eq. (15), $J_{sol} = -J_{an}$ on the anode side and $J_{sol} = J_{cat}$ on the cathode side. For Eq. (16), $J_{mem} = J_{an}$ on the anode side and $J_{mem} = -J_{cat}$ on the cathode side. The proton conductivity, σ_{mem}, is calculated as:

$$\sigma_{mem} = (0.514\lambda - 0.326) \exp \left[1268 \left(\frac{1}{303} - \frac{1}{T} \right) \right] \tag{17}$$

where λ is the membrane water content described as [12]:

$$\lambda = \begin{cases} 0.043 + 17.18a - 39.85a^2 + 36a^3 & 0 < a \leq 1 \\ 14 + 1.4(a - 1) & 1 < a \leq 3 \\ 16.8 & a > 3 \end{cases} \tag{18}$$

where a is the water activity defined as:

$$a = \frac{p_{wv}}{p_{sat}} + 2s \tag{19}$$

where p_{wv} is the water vapor pressure computed as $p_{wv} = X_{H_2O}p$. Here X_{H_2O} is the mole fraction of water vapor, p is the local pressure. The saturation pressure, p_{sat}, is computed as:

$$\begin{aligned} \log_{10} p_{sat} =\ & -2.1794 + 0.02953(T - 273.17) \\ & - 9.1837 \times 10^{-5}(T - 273.17)^2 \\ & + 1.4454 \times 10^{-7}(T - 273.17)^3 \end{aligned} \tag{20}$$

Table 3
Operating conditions of validation cases.

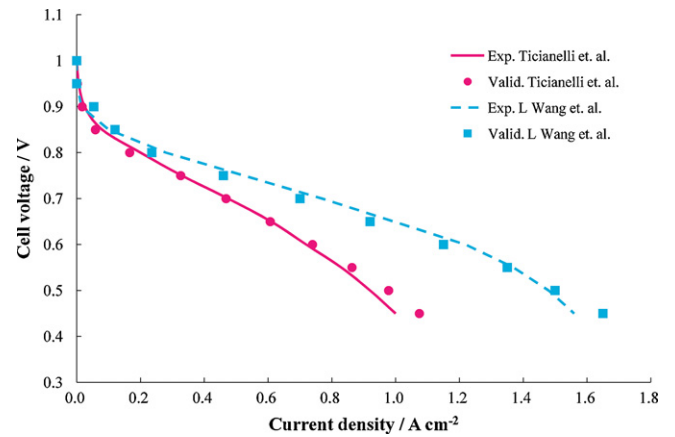|	Case Ticianelli	Case Wang
Anode		
Gas	H$_2$	H$_2$
Flow rates (kg s^{-1})	1.45×10^{-7}	1.80×10^{-6}
Inlet temperature (K)	353	343
Relative humidity (%)	0	100
Back pressure (atm)	3.0	3.0
Cathode		
Gas	Air	Air
Flow rates (kg s^{-1})	8.26×10^{-6}	4.73×10^{-5}
Inlet temperature (K)	353	343
Relative humidity (%)	100	100
Back pressure (atm)	5.0	3.0
Operating conditions		
Operating pressure (atm)	1.0	1.0
Cell temperature (K)	343	343

Fig. 2. Comparison of experimental and simulated polarization curves.

Liquid water formation and transport can be expressed by the following generalized Richards equation [13]:

$$\begin{aligned} & \nabla \cdot \left(\frac{\rho_l \kappa_p s^3}{\mu_l} \frac{\partial p_c}{\partial s} \nabla s \right) - \nabla \cdot \left(\frac{\rho_l \kappa_p s^3}{\mu_l} \nabla p_g \right) \\ & + \nabla \cdot \left(\frac{n_d M_{H_2O}}{F} \vec{i}_m \right) = S_m \end{aligned} \tag{21}$$

where ρ_l is the liquid water density, μ_l is the liquid water viscosity, $\vec{i}_m$ is the ionic current and n_d is the osmotic drag coefficient defined as $n_d = 2.5(\lambda/22)$ [12]. The capillary pressure, p_c, is computed as a function of s,

$$p_c = \begin{cases} \tau \cos \theta_c \left(\frac{\varepsilon}{\kappa_p} \right)^{0.5} [1.417(1-s) - 2.12(1-s)^2 + 1.263(1-s)^3] & \theta_c > 90° \\ \tau \cos \theta_c \left(\frac{\varepsilon}{\kappa_p} \right)^{0.5} (1.417s - 2.12s^2 + 1.263s^3) & \theta_c < 90° \end{cases} \tag{22}$$

where τ is the surface tension, θ_c is the contact angle of water on the porous medium.

The source terms in Eqs. (1), (5) and (21), is defined as follows [14]:

$$S_m = \begin{cases} M_{H_2O}\kappa_c \dfrac{\varepsilon(1-s)X_{H_2O}}{RT}(p_{H_2O} - p_{sat}) & \text{if } p_{H_2O} > p_{sat} \\ \kappa_e \varepsilon s \rho_l (p_{H_2O} - p_{sat}) & \text{if } p_{H_2O} < p_{sat} \end{cases} \tag{23}$$
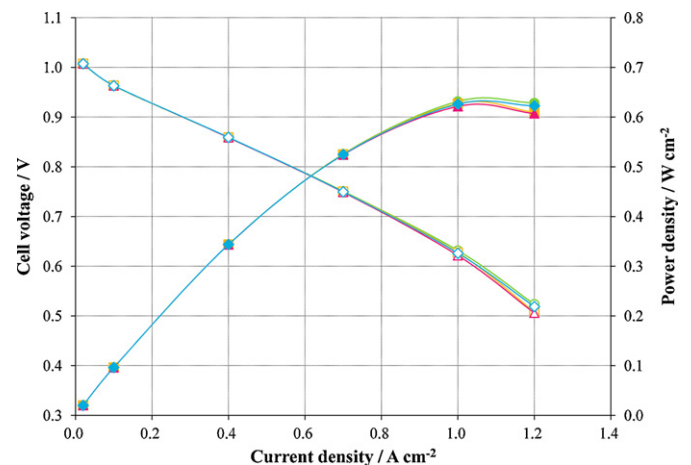

Fig. 3. Polarization (not filled) and power density (filled) curves of these four flow-fields configuration at high inlet humidity: A-0 (○); A-90 (△); A-180 (□); A-270 (◇).
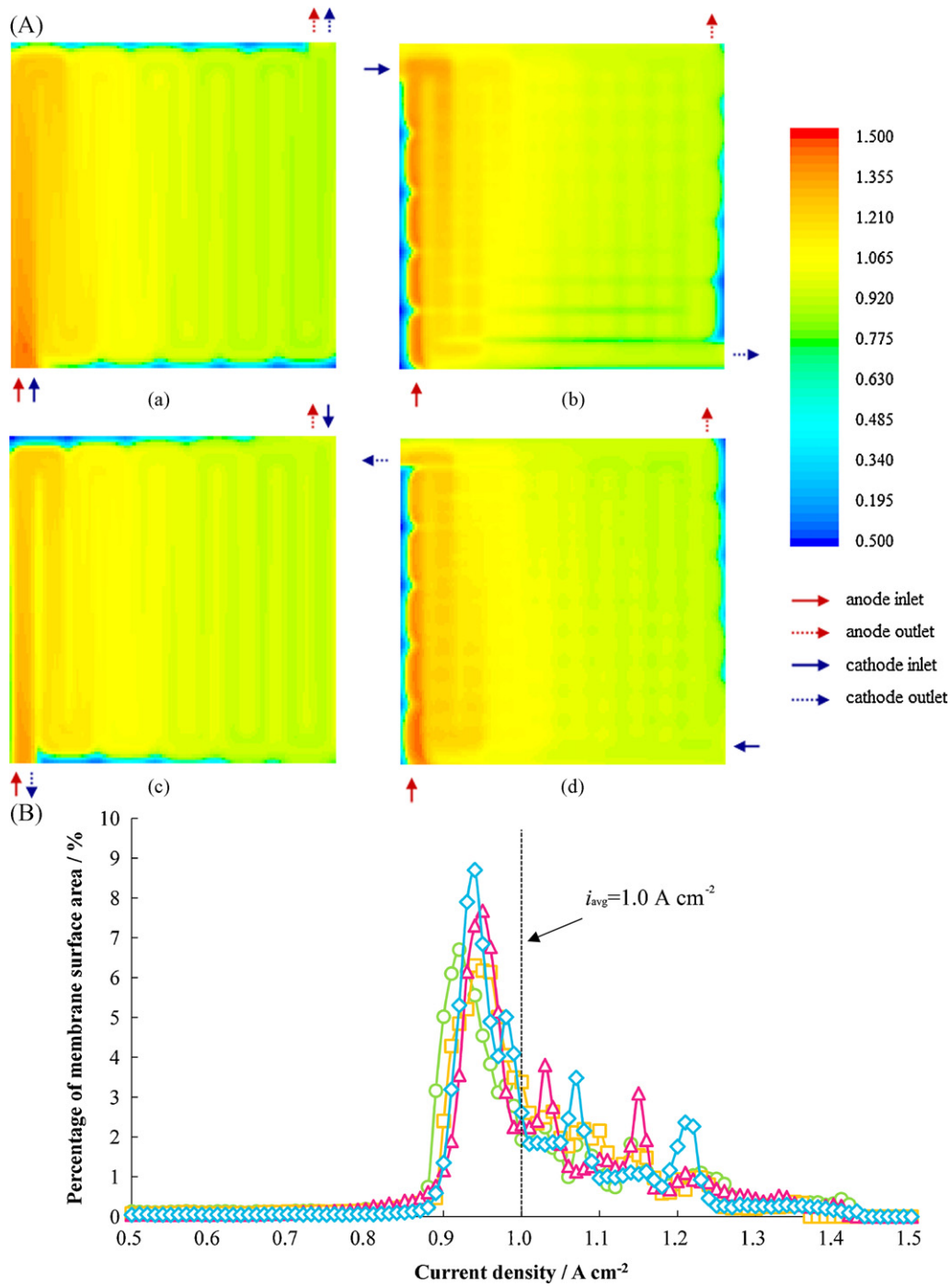
Fig. 4. (A) Current density (A cm^{-2}) distributions on membrane surface at I_{avg} = 1000 mA cm^{-2} and high inlet humidity: (a) A-0; (b) A-90; (c) A-180; (d) A-270. (B) Percentage of membrane surface area along current density at I_{avg} = 1000 mA cm^{-2} and high inlet humidity: A-0 (○); A-90 (△); A-180 (□); A-270 (◇).

where κ_c is the coefficient of water vapor condensation rate, κ_e is the coefficient of water vapor evaporation rate.

The generated water at the cathode side results in a gradient of water content between the anode and cathode sides of the membrane. This gradient can cause a water flux back to anode side. This back diffusion flux, D_b^{diff}, is described as follows:

$$D_b^{diff} = -\frac{\rho_{mem}}{M_{mem}} M_{H_2O} D_m \nabla \lambda \qquad (24)$$

where ρ_{mem} and M_{mem} are the density and equivalent weight of the dry membrane, respectively. The membrane water diffusivity, D_m,

is expressed as follows [15]:

$$D_m = 10^{-10} D'_m \exp\left[2416\left(\frac{1}{303} - \frac{1}{T}\right)\right] \qquad (25)$$

$$D'_m = \begin{cases} 1.0 & \lambda < 2 \\ 1 + 2(\lambda - 2) & 2 \leq \lambda \leq 3 \\ 3 - 1.67(\lambda - 3) & 3 \leq \lambda \leq 4.5 \\ 1.25 & \lambda \geq 4.5 \end{cases} \qquad (26)$$

Table 4
Conclusions of statistical results at 1000 mA cm^{-2} under high and low humidity conditions.

	A-0	A-90	A-180	A-270
High inlet humidity				
Standard deviation of current density (mA cm^{-2})	183	173	168	158
Average value of membrane water content	11.39	11.42	11.37	11.38
Standard deviation of membrane water content	2.50	2.62	2.60	2.61
Low inlet humidity				
Standard deviation of current density (mA cm^{-2})	208	256	188	203
Average value of membrane water content	8.46	8.62	8.13	8.23
Standard deviation of membrane water content	3.28	3.22	3.57	3.35
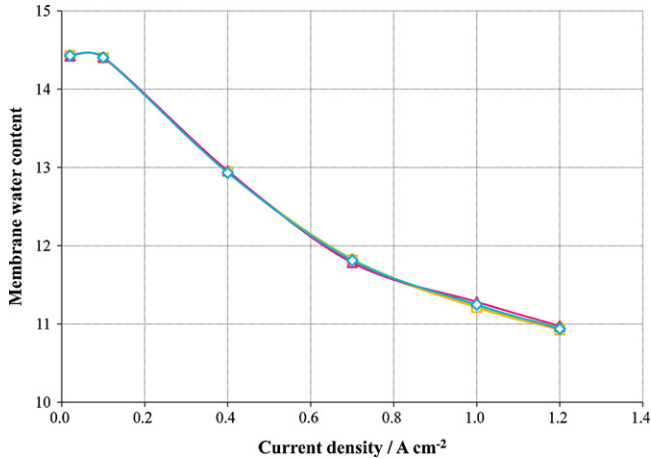
Fig. 5. Average membrane water content of these four flow-fields configuration at high inlet humidity: A-0 (◯); A-90 (△); A-180 (□); A-270 (◇).

The thermal energy equation is as follows [16]:

$$\nabla \cdot [\varepsilon(1-s)\rho_g \vec{u}_g C_{p,g} T] + \nabla \cdot (\varepsilon s \rho_l \vec{u}_l C_{p,l} T)$$

$$= \nabla \cdot (\kappa_{eff} \nabla T) + J_{echm} + \frac{i^2}{\sigma} + h_w S_m \tag{27}$$

where $C_{p,g}$ and $C_{p,l}$ are the specified heat of gaseous and liquid phases, κ_{eff} is the effective thermal conductivity, h_w is the enthalpy of formation for water. The last three terms on the right in Eq. (27) present electrochemical effect, Joule heating and latent heat based on the phase change, respectively.

2.2. Geometry and operations

The fuel cell model included the anode current collector, anode flow channel, anode gas diffusion layer, anode catalyst layer, proton exchange membrane, cathode catalyst layer, cathode gas diffusion layer, cathode flow channel and cathode current collector. The full-cell computational models had dimensions of 22 mm (length) × 22 mm (width) × 3.758 mm (height). In this work, channel assembled angle was defined as shown in Fig. 1(B). Four computational models with channel assembled angles of 0°, 90°, 180° and 270° were built (see in Fig. 1(A)), and were named A-0, A-90, A-180 and A-270 respectively for simply identified. In addition, considering the flow-field configurations observed in the top view, case A-0 and -180 can be grouped as channel-overlapping flow-fields, while A-90 and -270 are channel-perpendicular flow-fields. Table 1 summarizes the geometry details and material properties in the simulation. The inlet flow rates and gaseous mixture compositions at the anode and cathode inlets were assumed constant. Operating conditions and parameters are listed in Table 2.
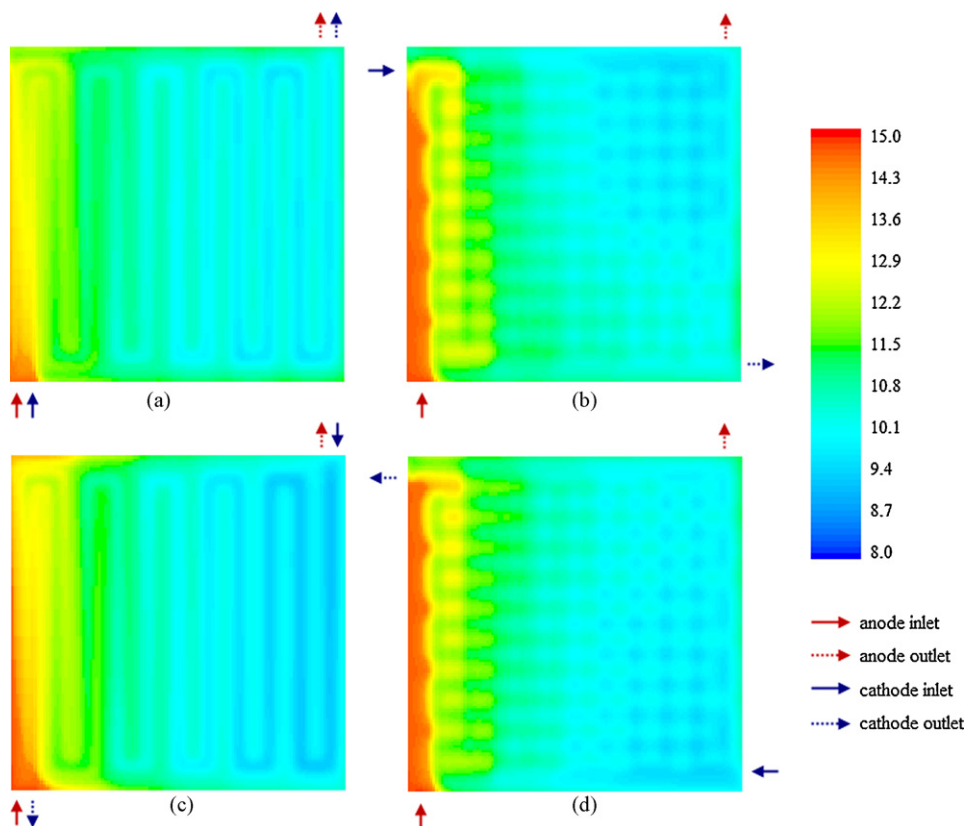

Fig. 6. Membrane water content distributions on membrane surface at I_{avg} = 1000 mA cm^{-2} and high inlet humidity: (a) A-0; (b) A-90; (c) A-180; (d) A-270.
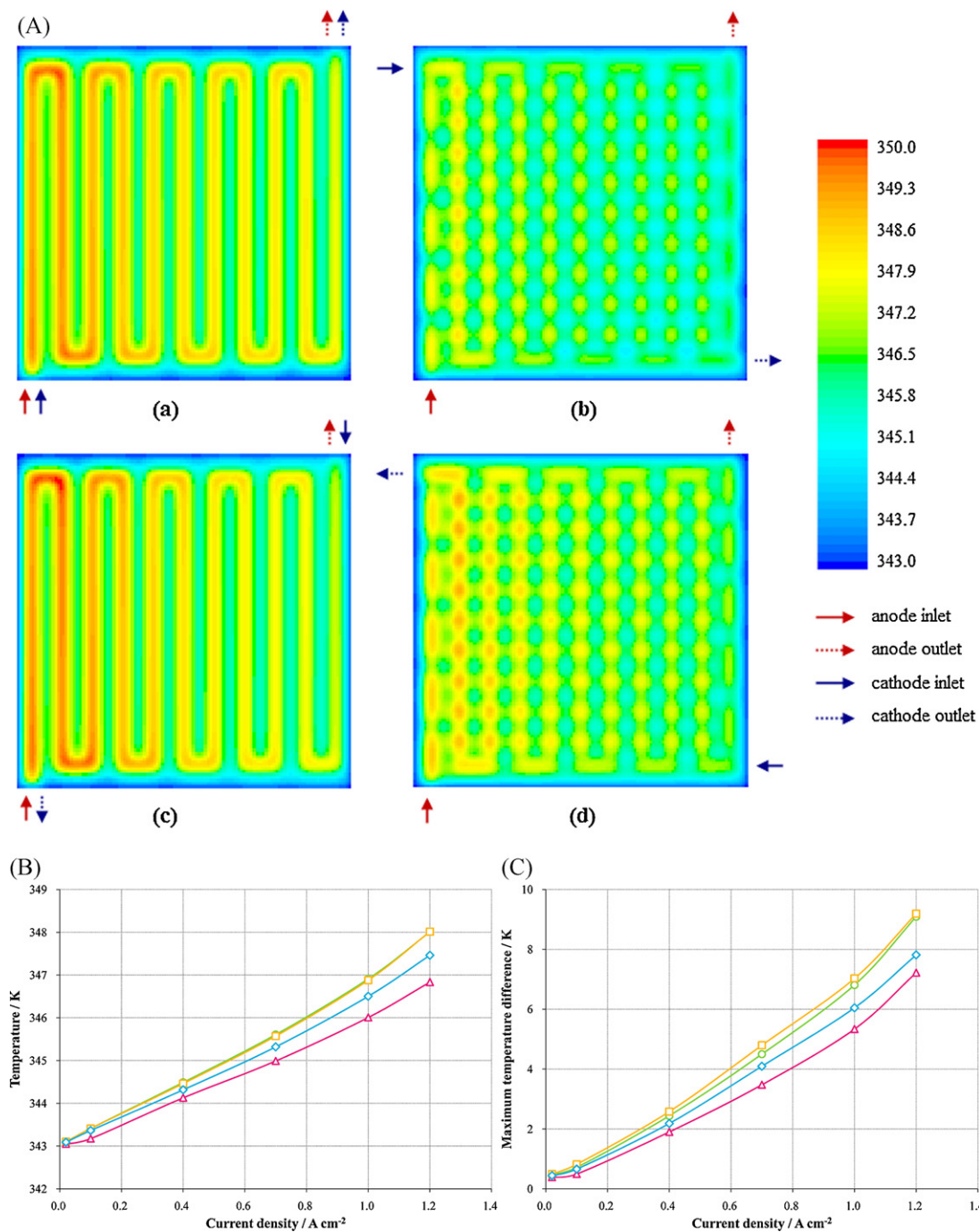
Fig. 7. (A) Local temperature (K) distributions on anode membrane surface at I_{avg} = 1000 mA cm^{-2} and high inlet humidity: (a) A-0; (b) A-90; (c) A-180; (d) A-270. (B) Average temperature on anode membrane surface of these four flow-fields configuration at high inlet humidity: A-0 (○); A-90 (△); A-180 (□); A-270 (◇). (C) Maximum temperature difference on anode membrane surface of these four flow-fields configuration at high inlet humidity: A-0 (○); A-90 (△); A-180 (□); A-270 (◇).

2.3. Numerical procedure

The coupled governing equations were solved using FLUENT, a CFD package based on the finite volume technique. The numerical scheme for solving the flow-fields was a pressure-based segregated algorithm, SIMPLE, with aggregative algebraic multigrid (AAMG) method. In order to improve convergence, biconjugate gradient stabilized method (BCGSTAB) was used to solve the species and potential equations. The calculation was completed with double precision for the accurate results. Convergence criterion for all equations was 1e−07 except the energy equation, for which was set at 1e−10. Structured and uniform grid cells were used

to mesh the models. Considering the predictable complex effects caused by the channel "cross-sections" in channel-perpendicular flow-fields, refined mesh schemes were established in these models. For obtaining comparable results, channel-overlapping models were meshed by the same scheme, although they can be treated with fewer cells. Therefore, all models were divided into 126 (length) × 124 (width) × 53 (height) structured grid cells, and the total cell number was about 830,000. Grid independence was tested before the simulation. The number of grid cells of case A-0 was increased and decreased by 50%, and difference between the cases were predicted less than 5%. As a result, the present mesh scheme can be concluded as grid independence. The numerical models were

validated by comparing previous work of Ticianelli et al. [17] and Wang et al. [18], whose experiments were carried out in single cells with active surface area of 5 and 51.84 cm² , respectively. Operating conditions are listed in Table 3. Fig. 2 shows that the numerical results agreed well with the experiment data.

3. Results and discussion

3.1. High inlet humidity

Fig. 3 shows the polarization and power density curves of the four flow-fields under high inlet humidity condition. As the average current density increased, the cell voltage decreased because of the increase of overall potential loss. The four flow-fields perform almost the same over all regions. Even in the mass transfer limited region (i.e. cell voltages below 0.6 V) the difference between the highest case (i.e. case A-0) and the lowest one (i.e. case A-90) is just under 3.5% for cell voltage, or 3.3% for power density. This similarity could be due to the same size of the active area, the same operating condition and inlet condition. Therefore, changing the channel assembled angle has little influence on the polarization and output power density.

Fig. 4(A) shows current density distribution on membrane surface for all flow-fields at 1000 mA cm⁻². The cell voltage of case A-0, -90, -180 and -270 are 0.632, 0.622, 0.627 and 0.626 V, respectively. It reveals that the difference of cell performance among these flow-fields is just around 1.6%. Because of high reactant concentration and reaction rate, local current density is high near the anode inlet. Then it becomes more uniform in the middle of the flow-field and maintains that level till the exit. The current density is higher under the ribs than under the channel regions. It is because the lower temperature under the ribs can reduce the saturation pressure of water and increase membrane water content, which results in raising the local performance [1].

In numerical simulation, the computational model is discretized into thousands of small meshes, and then the governing equations are solved by suitable algorithms. After the calculation, each mesh has its own result. Statistical theory is a useful tool to sum up the results of the meshes into a brief conclusion, and to make it possible to present or compare some physical properties (e.g. distribution, uniformity, etc.) in quantity.

Nonuniform current density distribution in PEM fuel cell can induce local variations in the membrane conductivity, cell temperature and water concentration, which can cause stresses on the membrane and reduce the lifetime of the cell. Here statistical theory is employed to determine the uniformity of current density distribution. Table 4 shows that at 1000 mA cm⁻² the standard deviation of current density of case A-0, -90, -180 and -270 are 183, 173, 168 and 158 mA cm⁻², respectively. A lower standard deviation reveals that the current density distribution tends to be more uniform. The percentage of membrane surface area together with the current density at 1000 mA cm⁻² is presented in Fig. 4(B). For all flow-fields, the current density on membrane surface mainly ranges from 800 to 1450 mA cm⁻². But in the range around average value (i.e. from 900 to 1100 mA cm⁻²), the A-0, -90, -180 and -270 flow-fields have total percentages of 66.9, 66.8, 73.5 and 73.6%, respectively. The results explain why those cases A-180 and -270 have lower standard deviations than the other two. Furthermore, outside the major range (i.e. below 800 mA cm⁻²) case A-270 has a total percentage of 3.4%, which is less than 5.8% of case A-180. This results in case A-270 having a lower standard deviation than A-180. On the other hand, case A-90 has a total percentage of 40.3% from 950 to 1050 mA cm⁻², which is higher than the 29.6% of case A-0. Moreover, compared with a total percentage of 6.6% of case A-0 below 800 mA cm⁻², case A-90 has a lower value of 4.5%. There-
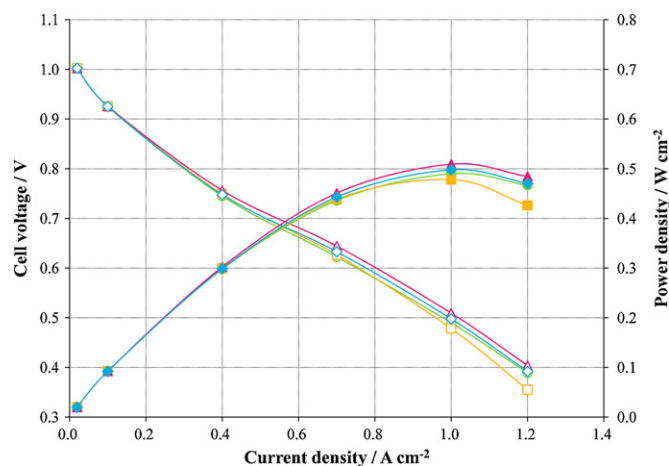

Fig. 8. Polarization (not filled) and power density (filled) curves of these four flow-fields configuration at low inlet humidity: A-0 (○); A-90 (△); A-180 (□); A-270 (◇).

fore case A-90 shows a lower standard deviation than that of case A-0. In conclusion, case A-270 has most uniform current density distribution.

The membrane water content indicates the hydration state of membrane, which is relative to the membrane resistance and conductivity. Fig. 5 shows the average membrane water content as function of current density. The four curves almost coincide because they have the same operating conditions which have been explained before. As current density increases, more water transports from anode to cathode and the membrane water content decreases. As a result, the membrane becomes dry because the hydration state of the membrane is a stronger function of anode water activity than cathode water activity [19]. For all flow-fields the membrane water content is above 14.0 at low current density. It implies that at low current density all flow-fields have considerable fraction of liquid water, which is close related to the temperature and humidity conditions. The existence of liquid water could reduce the performance of the cell.

Fig. 6 displays membrane water content distribution on membrane surface at 1000 mA cm⁻². The membrane water content is higher near the anode inlet regions and becomes more uniform in a quarter of the flow-field. This is because under high inlet humidity condition, large mole fraction of water exists at the anode inlet region, causing high concentration difference that makes water transfer from anode to cathode. Moreover, for channel-overlapping flow-fields, because channel regions in anode and cathode are overlapped, water can easily transfer from anode to cathode. But for channel-perpendicular flow-fields, the anode channel only cross discontinuous regions of cathode channel, which makes water transfer less to the cathode but keep more within the membrane. Consequently, as seen in Fig. 6, larger regions of high membrane water content exist near the anode inlet of the channel-perpendicular flow-fields than that of channel-overlapping ones.

Uniform distribution of membrane water content can extend the lifetime of PEM fuel cell. Table 4 shows that the A-0, -90, -180 and -270 flow-fields have average membrane water content of 11.39, 11.42, 11.37 and 11.38, respectively. The difference between the highest (i.e. case A-90) and the lowest value (i.e. case A-180) is only 0.05, or 0.44%, which reveals that there is little difference for membrane water content among the four flow-fields at high inlet humidity condition. The standard deviation of A-0, -90, -180 and -270 are 2.50, 2.62, 2.60 and 2.61, respectively. As seen in Fig. 6, the difference in standard deviations is mostly caused by the difference of membrane water content at the entrance regions as discussed
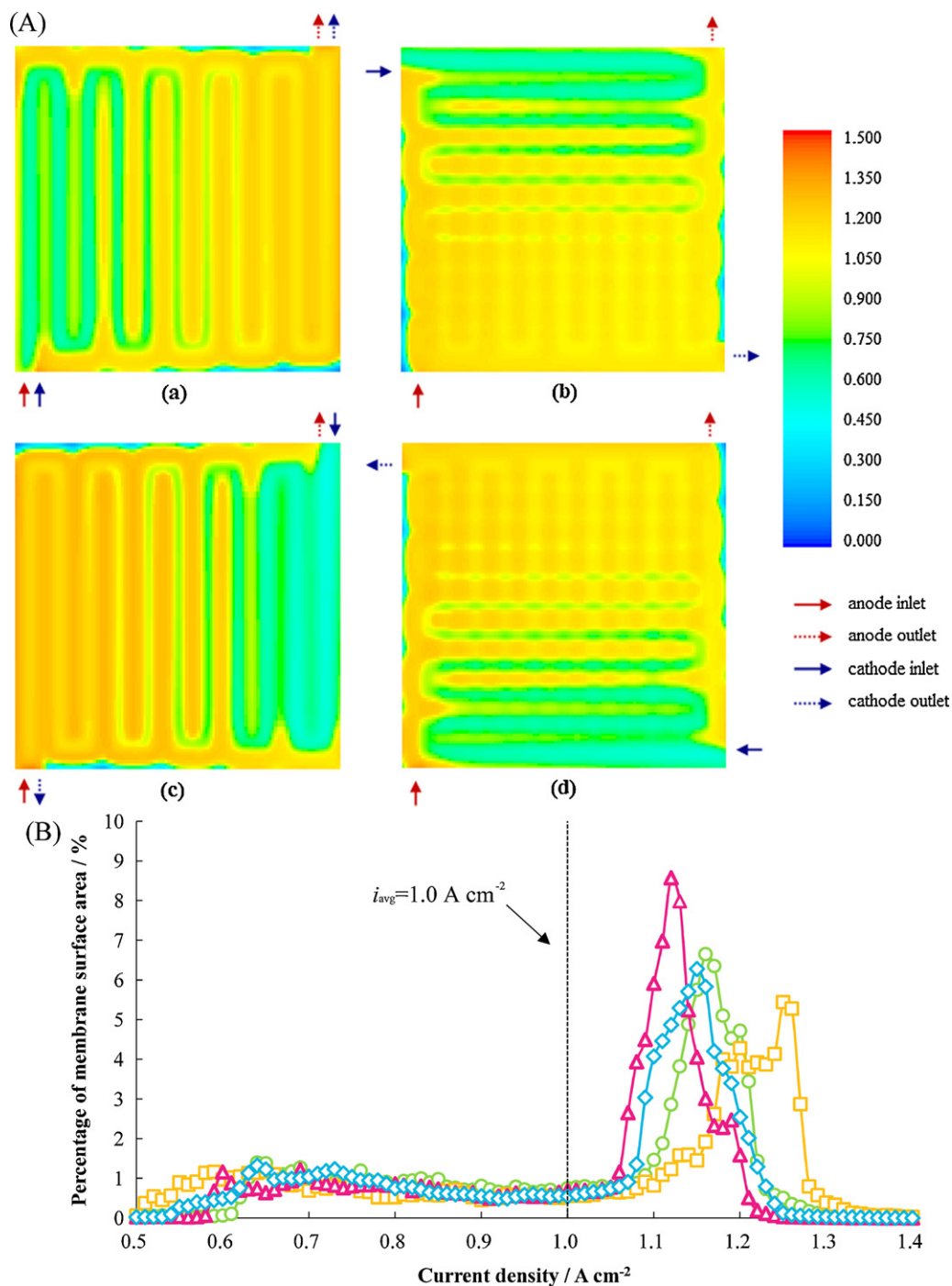
Fig. 9. (A) Current density (A cm^{-2}) distributions on membrane surface at I_{avg} = 1000 mA cm^{-2} and low inlet humidity: (a) A-0; (b) A-90; (c) A-180; (d) A-270. (B) Percentage of membrane surface area along current density at I_{avg} = 1000 mA cm^{-2} and low inlet humidity: A-0 (○); A-90 (△); A-180 (□); A-270 (◊).

before. Case A-0 shows more uniform in membrane water content than the others.

The distribution of reaction rate across the electrode surface causes distributions in temperature and other electrochemical variables in a PEM fuel cell. Fig. 7(A) displays the local temperature distribution on the anode membrane surface at 1000 mA cm^{-2}. For all flow-fields, temperature is higher near the anode inlet, and drops along the anode channel from inlet to outlet. This phenomenon indicates that in these simulations the reactant concentration on anode side has considerable effect on the reaction rates. There are many hot spots distributing over the surfaces of case A-90 and -270 because they locate on the intersection of anode and cathode

channels, where reaction rate is higher than other regions. The standard deviation of temperature of A-0, -90, -180 and -270 are 1.67, 1.70, 1.10 and 1.20 K, respectively. Thus case A-90 has most uniform temperature distribution. This could be due to the appropriate matching of reactant concentrations caused by the special channel configuration. Another phenomenon is the temperature adjacent to the rib areas is lower than that under the channels. This could be due to two reasons. One is that the location under the channel is the main reaction region because it has higher reactant concentration. The other reason is that heat generated in the region under the ribs can be more easily transferred than that produced under the channels.
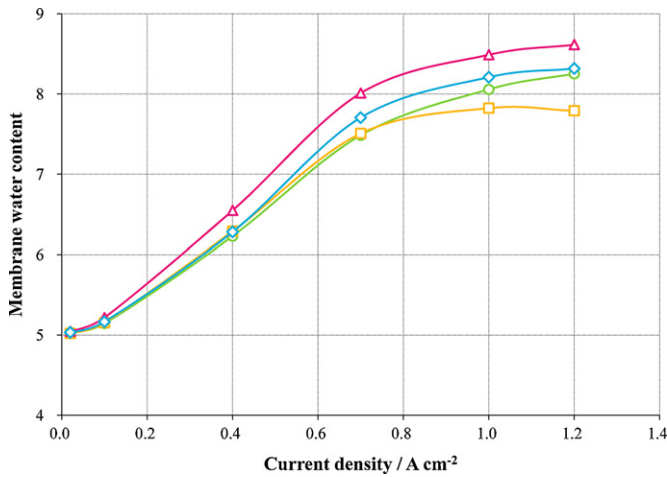
Fig. 10. Average membrane water content of these four flow-fields configuration at low inlet humidity: A-0 (○); A-90 (△); A-180 (□); A-270 (◇).

that the channel-perpendicular flow-fields have smaller temperature ranges than channel-overlap ones. As seen in Fig. 7(A), the channel-overlap cases have continuous high temperature regions from the inlets to outlets, while the channel-perpendicular ones just have discontinuous hot spots, from which the generated heat can spread out more easily.

3.2. Low inlet humidity

Fig. 8 shows the polarization and power density curves of the four flow-fields at low inlet humidity condition. The four cases present similar performance at low current density, but at current density above $400\,mA\,cm^{-2}$ the difference becomes obvious. Case A-90 shows best performance while case A-180 presents the worst. At high current density region the difference between these two cases can reach 13.6% for cell voltage and 13.8% for power density. Compared with that under high inlet humidity condition, results at low inlet humidity condition reveal that changing channel assembled angle have considerable effect on the cell performance.

Fig. 9(A) shows current density distribution on membrane surface at $1000\,mA\,cm^{-2}$. Case A-90 has a higher cell voltage than other flow-fields. Case A-0, -90, -180 and -270 give cell voltages of 0.490, 0.509, 0.478 and 0.498 V, respectively. For all flow-fields the local current density is low at cathode inlet regions. This could be due to the high membrane resistance caused by low membrane water content over these regions at low inlet humidity condition. Furthermore, current density becomes higher from the middle of the flow-fields to the cathode outlets because higher membrane water content in these regions reduces the membrane resistance (will be discussed later).
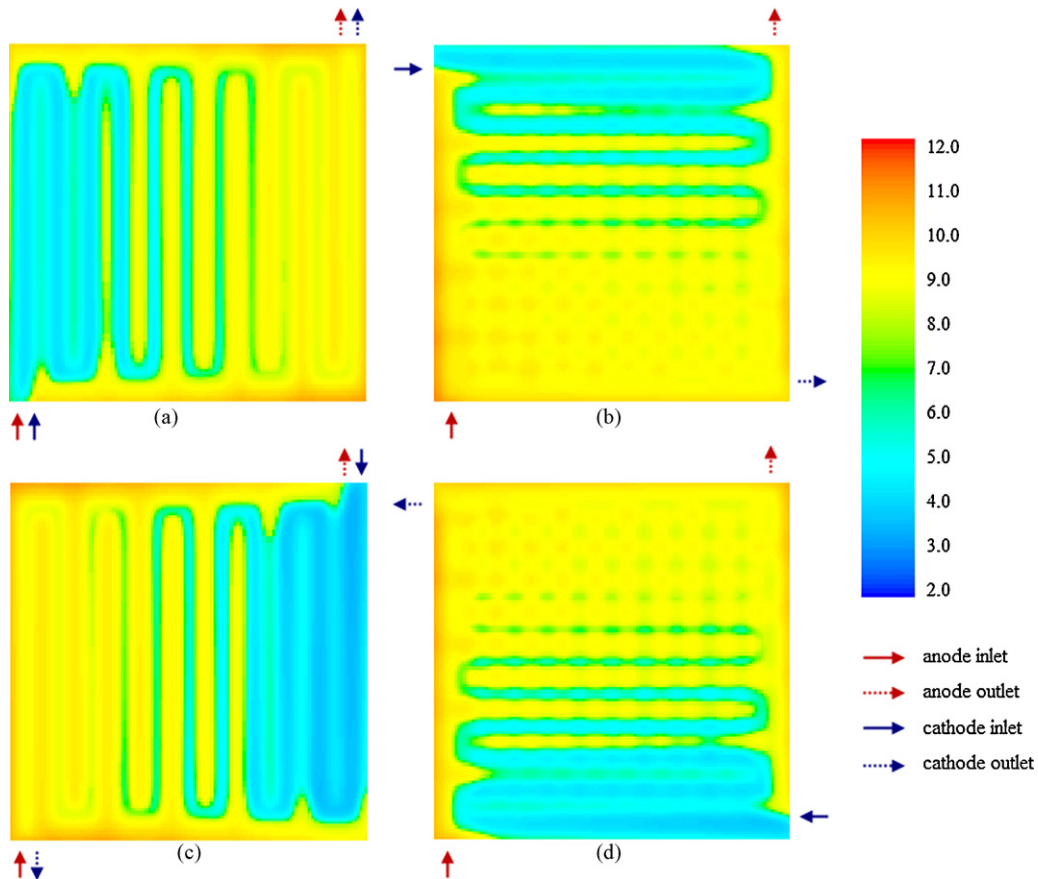
Fig. 7(B) shows the average temperature on the anode membrane surface at each current density. The temperature increases with increase of average current density because of higher reaction rate. The curves of case A-0 and -180 almost overlap but obviously A-90 and -270 present lower values, although all flow-fields have similar performance on polarization curves as seen in Fig. 3. This discrepancy could be due to the local temperature distribution as discussed before. Fig. 7(C) shows the temperature difference between the maximum and minimum local temperatures as a function of the average current density. It can be observed

Fig. 11. Membrane water content distributions on membrane surface at $I_{avg} = 1000\,mA\,cm^{-2}$ and low inlet humidity: (a) A-0; (b) A-90; (c) A-180; (d) A-270.
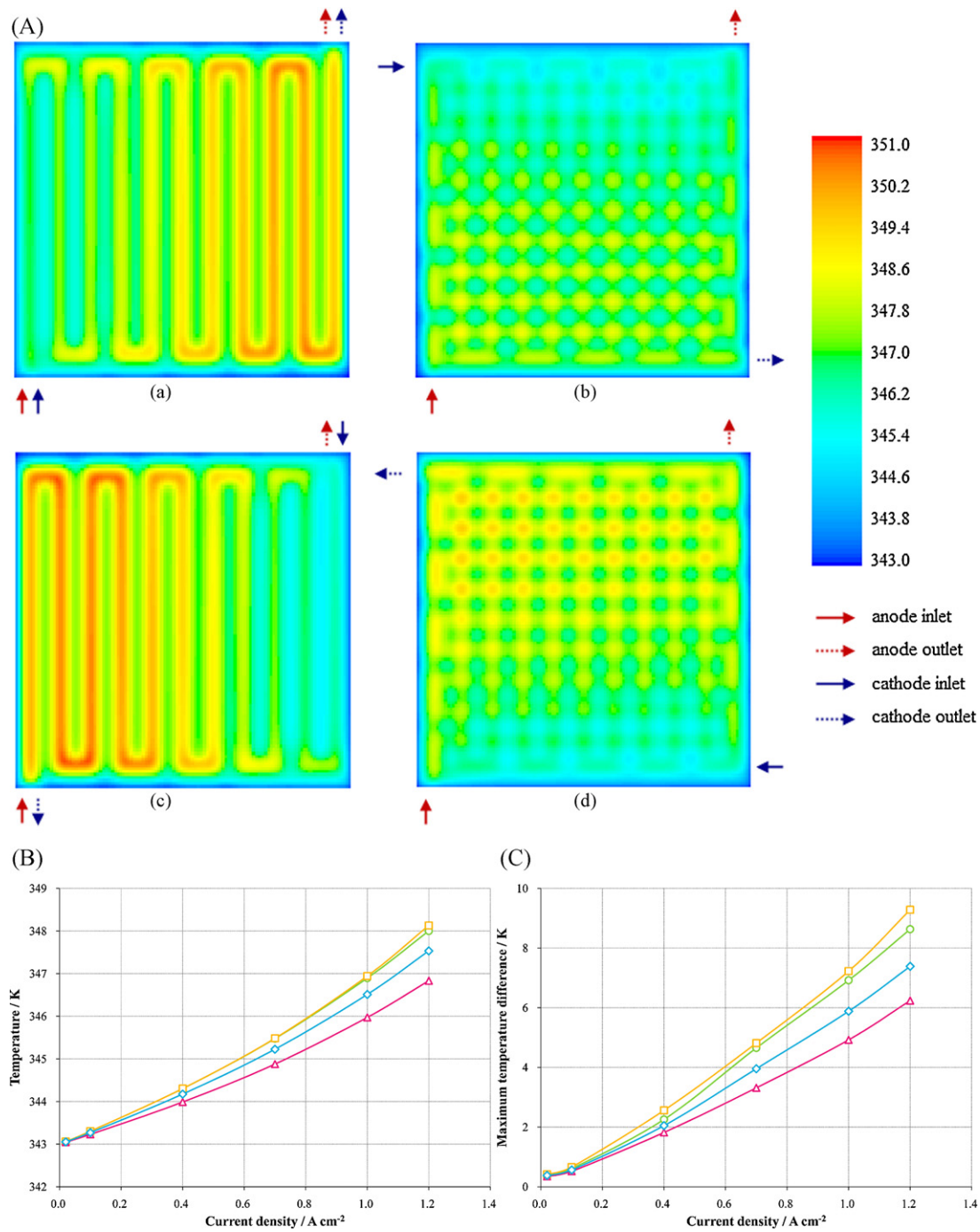
Fig. 12. (A) Local temperature (K) distributions on anode membrane surface at $I_{avg} = 1000\,\text{mA cm}^{-2}$ and low inlet humidity: (a) A-0; (b) A-90; (c) A-180; (d) A-270. (B) Average temperature on anode membrane surface of these four flow-fields configuration at low inlet humidity: A-0 (○); A-90 (△); A-180 (□); A-270 (◇). (C) Maximum temperature difference on anode membrane surface of these four flow-fields configuration at low inlet humidity: A-0 (○); A-90 (△); A-180 (□); A-270 (◇).

Table 4 shows that at $1000\,\text{mA cm}^{-2}$ the standard deviation of current density of A-0, -90, -180 and -270 are 208, 256, 188 and $203\,\text{mA cm}^{-2}$, respectively. It indicates that current density in case A-90 distributes more uniform than the others. Fig. 9(B) presents the percentage of membrane surface area together with the current density. For all flow-fields, the range between 500 and $1050\,\text{mA cm}^{-2}$ has a total percentage of 36–40% which reflects the low current density region near the inlet. Case A-90 has a total percentage of 64% distributes in the region from 1050 to $1250\,\text{mA cm}^{-2}$, which is narrowest and nearer to the average value than the others. This can explain why case A-90 has lowest standard deviation.

Fig. 10 shows the average membrane water content as function of current density under low inlet humidity condition. Different from that at high humidity condition, the membrane water content increases as current density increases. This occurs because less water exists at low current densities for humidifying the membrane under low humidity condition. As the current density increases, more water is generated in the cathode side and transport to the anode due to the concentration gradient, and then humidifies the membrane. Fig. 10 reveals that case A-90 has a better flow-field configuration to keep more water in the membrane to reduce the membrane resistance than the other cases.

Fig. 11 shows membrane water content distribution on membrane surface at 1000 mA cm^{-2}. For all flow-fields the membrane water content is low near the cathode inlet because of the low inlet humidity. In the middle of the surface, more water is generated and transports back from cathode to anode due to the strong back diffusion [20]. Membrane water content becomes uniform earlier (i.e. near 1/2 of the surface) in channel-perpendicular flow-fields than channel-overlapping ones (i.e. near 3/4 of the surface). This is because the special channel configurations in channel-perpendicular flow-fields makes more water stay in the membrane than transfer into the channels and drain away, then, reduces the membrane resistance. Table 4 shows that the A-0, -90, -180 and -270 flow-fields have average membrane water content of 8.46, 8.62, 8.13 and 8.23, respectively. And standard deviations are 3.28, 3.22, 3.57 and 3.35, respectively. The data indicates that case A-90 has a higher average value of membrane water content and a more uniform water content distribution than others.

Fig. 12(A) shows the local temperature distribution on the anode membrane surface at 1000 mA cm^{-2}. For all flow-fields the temperature increases along the cathode channel from the inlet to outlet because the increasing reaction rate which is close related to the distribution of current density and membrane water content, as discussed before. The standard deviation of temperature of A-0, -90, -180 and -270 are 1.61, 1.04, 1.78 and 1.22 K, respectively. It indicates that flow-field A-90 has most uniform temperature distribution at low inlet humidity condition.

Fig. 12(B) and (C) shows the average value and maximum difference of temperature on the anode membrane surface at each current density, respectively. As the results discussed at high inlet humidity condition, both average value and maximum difference of temperature increase as the average current density increases. Owe to the appropriate channel configuration, case A-90 shows best performance on temperature difference.

4. Conclusion

This paper used a three-dimensional, two-phase, multi-component model to investigate the effects of channel assembled angle on the performance of PEM fuel cell. Distributions of current density, membrane water content and local temperature in four flow-fields, which was installed based on the single serpentine pattern with different assembled angles (i.e. 0°, 90°, 180° and 270°), were analyzed under two humidity conditions.

It is concluded that changing flow-field configuration by varying channel assembled angle can affect its uniformity. For high inlet humidity, there were little difference on polarization and membrane water content among the four flow-fields. Case A-0 showed most uniform membrane water content, but just 5% higher than the lowest case. Moreover, case A-270 had most uniform current density distribution, while case A-90 had most uniform local temperature distribution. It can be summarized that each flow-field had its owned strengths at high inlet humidity. However, for low inlet humidity, due to the appropriated flow-field configuration, case A-90 represented obvious advantages in polarization and performance. It also showed most uniform distributions in current density, membrane water content and temperature. Therefore, channel assembled angles is one of the factors that should be considered in optimizing the performance, efficiency and durability in PEM fuel cell design.

References

[1] S. Shimpalee, S. Greenway, J.W. Van Zee, J. Power Sources 160 (2006) 398–406.
[2] D.H. Jeon, S. Greenway, S. Shimpalee, J.W. Van Zee, Int. J. Hydrogen Energy 33 (2008) 1052–1066.
[3] X. Li, I. Sabir, Int. J. Hydrogen Energy 30 (2005) 359–371.
[4] S. Fell, J. Roth, B. Steidle, D. Baker, W. Gu, M. Mathias, et al., VDI Berichte (2002) 579–600.
[5] J. Glandt, S. Shimpalee, W.K. Lee, J.W. Van Zee, AIChE's 2002 Spring National Meeting, New Orleans, LA, 2002.
[6] G. Hu, J. Fan, S. Chen, Y. Liu, K. Cen, J. Power Sources 136 (2004) 1–9.
[7] A. Su, Y.C. Chiu, F.B. Weng, Int. J. Energy Res. 29 (2005) 409–425.
[8] P.W. Li, S.P. Chen, M.K. Chyu, J. Power Sources 140 (2005) 311–318.
[9] S. Karvonen, T. Hottinen, J. Saarinen, O. Himanena, J. Power Sources 161 (2006) 876–884.
[10] J.P. Kloess, X. Wang, J. Liu, Z. Shi, L. Guessous, J. Power Sources 188 (2009) 132–140.
[11] T. Berning, D. Lu, N. Djilali, J. Power Sources 106 (2002).
[12] T.E. Springer, T.A. Zawodzinski, S. Gottesfeld, J. Electrochem. Soc. 138 (1991) 2334–2342.
[13] X.D. Wang, X.X. Zhang, W.M. Yan, D.J. Lee, A. Su, Int. J. Hydrogen Energy 34 (2009) 3823–3832.
[14] S. Mazumder, J.V. Cole, J. Electrochem. Soc. 150 (2003) A1510–A1517.
[15] S. Shimpalee, D. Spuckler, J.W. Van Zee, J. Power Sources 167 (2007) 130–138.
[16] X.D. Wang, Y.Y. Duan, W.M. Yan, D.J. Lee, A. Su, P.H. Chi, J. Power Sources 193 (2009) 684–690.
[17] E.A. Ticianelli, C.R. Derouin, A. Redondo, S. Srinivasan, J. Electrochem. Soc. 135 (1988) 2209–2214.
[18] L. Wang, A. Husar, T. Zhou, H. Liu, Int. J. Hydrogen Energy 28 (2003) 1263–1272.
[19] F.N. Büchi, G.G. Scherer, J. Electrochem. Soc. 148 (2001) A183–A188.
[20] S. Shimpalee, S. Greenway, D. Spuckler, J.W. Van Zee, J. Power Sources 135 (2004) 79–87.
[21] J.H. Nam, M. Karviany, Int. J. Heat Mass Transfer 46 (2003) 4595–4611.